Received: Added at production | Revised: Added at production | Accepted: Added at production

DOI: xxx/xxxx

RESEARCH ARTICLE

An idealised model of convective hydration of the Tropical Tropopause Layer. Part I: model formulation and diagnostic approach.

Charles W. Powell | **Peter H. Haynes** | **John R. Taylor**

[1]Department of Applied Mathematics and Theoretical Physics, University of Cambridge, Centre for Mathematical Sciences, Wilberforce Road, Cambridge, CB3 0WA

Correspondence
Corresponding author: Charles Powell.
Email: cwp29@cam.ac.uk

Abstract

Convection that overshoots the tropical cold point tropopause can irreversibly transport water vapour, providing an important pathway for hydration of the tropical lower stratosphere. We formulate an idealised model of this process by treating a convective overshoot as a buoyant plume penetrating a stably stratified layer carrying tracers that represent vapour and ice. We use large-eddy simulations to study a scaled-down model flow, which more faithfully represents small-scale turbulence compared to earlier numerical studies. The vapour and ice tracers evolve according to a minimal moisture model with equal and opposite rates of condensation and sublimation and a fixed sedimentation velocity for the ice tracer. We explore the behaviour of the model in two experiments where the sedimentation velocity and partitioning of moisture into vapour and ice is varied. To understand the influence of mixing we extend a formalism that captures the simultaneous modification of buoyancy and tracer concentration to include terms representing the effect of moist processes. We find that our model is an effective representation of the hydration mechanism observed in the tropical tropopause layer when the plume penetrates the stratified layer carrying large amounts of ice which are mixed with the warmer environment and sublimated to form vapour. Hydration of the stratified layer beyond the direct transport of vapour by the plume requires ice to remain in suspension during mixing in the plume cap, which is controlled by the relative sizes of the sedimentation velocity and turbulent eddy velocity.

KEYWORDS
Tropics, Stratosphere, Convection, Moisture, Numerical simulations, Turbulent mixing

1 | INTRODUCTION

Deep convection that overshoots the tropical cold-point tropopause (CPT) can avoid the cold-point constraint on water vapour concentrations, irreversibly transporting moisture into the tropical tropopause layer (TTL) where it may later rise into the tropical lower stratosphere on timescales of days to weeks (Jensen et al., 2007; Randel and Jensen, 2013; Jensen et al., 2020). Recent estimates using observational data and numerical simulations suggest that vertical moisture transport via convective penetration represents a second-order but non-negligible contribution of around 10–20% of water vapour mass input into the tropical lower stratosphere (Schoeberl et al., 2014; Dauhut et al., 2015; Ueyama et al., 2015, 2018; Dauhut and Hohenegger, 2022). Moisture anomalies formed in the tropical lower stratosphere (TLS) are communicated to the extratropics by the Brewer-Dobson circulation on timescales of a few years (Randel et al., 2004; Randel and Park, 2019), meaning convective hydration of the TTL plays an important role in determining water vapour concentrations in the stratosphere as a whole.

Convective penetration of the TTL occurs when particularly strong updrafts overshoot their level of neutral buoyancy, rising into the TTL and subsiding on timescales of tens of minutes. Typically, multiple overshoots are formed from longer-lived mesoscale convective systems (Rossow and Pearl, 2007). Convective penetration events are highly spatially inhomogeneous (Nugent and Bretherton, 2023) and short-lived, making observational studies difficult. Approaches such as Lagrangian trajectory modelling rely on cloud models and reanalysis datasets which are limited in resolution and accuracy. Numerical studies

using convection-resolving simulations of entire thunderstorm complexes have proved effective in identifying the mechanism of convective hydration of the TTL (e.g. Hassim and Lane (2010); Dauhut et al. (2015, 2018)). These studies have shown that convective hydration arises from turbulent mixing between cold, ice-rich air inside overshoots and the surrounding TTL environment that warms with height (Dauhut et al., 2018). Provided the TTL is subsaturated, the increased temperature of mixed air leads to sublimation of ice that locally increases the water vapour content. In cases where the TTL is supersaturated, ice-scavenging can instead lead to a dehydration of the TTL (Hassim and Lane, 2010). On longer timescales, slow quasi-horizontal upwelling lifts moisture from the TTL into the TLS. Gravity-wave associated temperature perturbations can temporarily cool anomalously moist regions during ascent, leading to the formation of ice which may sediment out of the TTL and reduce the amount of moisture that reaches the TLS (Wright et al., 2011; Pan et al., 2019; Khaykin et al., 2022).

Numerical studies using comprehensive meteorological models containing many physical processes are computationally expensive and can be challenging to interpret. The computational cost places a practical constraint on the number and length of simulations that can be considered, hence limiting the number of distinct convective penetration events and the breadth of environmental regimes considered. Further, whilst several numerical studies have investigated the role of turbulent mixing between overshooting tops and TTL air (Hassim and Lane, 2010; Dauhut et al., 2018; Sang et al., 2018), the grid scale of these convection-resolving simulations is typically well above turbulent length scales so their representation of turbulence heavily relies on sub-grid-scale parameterisations that may underestimate the importance of small-scale processes in driving mixing. Similarly, the use of detailed microphysical schemes may obfuscate the processes controlling convective hydration.

In this paper we formulate an idealised model for convective hydration of the TTL. We restrict focus to the transient process of hydrating the immediate surroundings of convective overshoots to form a moist anomaly in the TTL and do not consider the slow ascent occurring on longer timescales. Convective overshoots are modelled using a flow that is representative of convective penetration of the TTL, in which a turbulent buoyant plume generated in a uniform layer penetrates into a linearly stably stratified layer. Processes that occur as deep convective plumes rise through the troposphere are not considered important for convective hydration other than setting the conditions at penetration; by using a buoyant plume in our model we gain control on the conditions at penetration which are predictable according to the canonical Morton-Taylor-Turner axisymmetric plume equations (Morton et al., 1956). We consider large-eddy simulations of a scaled-down version of the geophysical problem, such that most of the turbulent spectrum is resolved, with the remainder parameterised by a sub-grid-scale scheme that has been shown to faithfully represent turbulent transport at the smallest scales (Abkar et al., 2016). Consequently, the scale at which energy is injected into the system by the plume is closer to the scale at which it is dissipated by turbulence, so our results are less sensitive to the sub-grid-scale model. We use a Boussinesq numerical scheme for simplicity, noting that the relevant processes occur in a shallow region where the plume penetrates into the stratified layer. In this region the density change is small and the dynamics are not dissimilar to a more complicated system without the Boussinesq approximation, even though the depth of the region of interest is not much smaller than the scale height.

To aid interpretation of the simulations and understanding of the mechanisms that contribute to convective hydration of the TTL, our model uses a minimal moisture scheme that retains only the moist species and microphysical processes thought to be relevant to the irreversible transport of water vapour. In particular, at its simplest, convective hydration can be understood in terms of the amount of vapour retained in convective lofted fluid parcels that penetrate into the TTL carrying large amounts of ice, mix with the TTL environment, and sublimate some of their ice content as the parcel warms. Consequently, the buoyant plume in our model carries only three tracers which are all passive in the sense that the tracer concentration does not influence the dynamics – latent heating is neglected owing to the small water vapour concentrations present in the TTL (Dauhut et al., 2018). Two temperature-dependent tracers represent water vapour and ice which are influenced by three parameterised microphysical processes: condensation of vapour to form ice, sublimation of ice to form vapour, and sedimentation of ice. A third 'fully passive' tracer evolves independent of moist processes or temperature and simply marks the extent of the plume. In pursuit of reduced complexity, we choose not to consider the influence of the humidity in the surrounding TTL environment, instead opting for a completely subsaturated TTL environment to simplify interpretation. We therefore focus exclusively on hydration of the TTL and do not consider the apparently less frequent dehydration events; this allows us to formulate a simpler model that does not represent supersaturation.

The main body of this paper is formed of three sections. First, in § 2, we detail the minimal moisture model, simulation setup, and define parameters used to quantitatively describe the regimes considered in each simulation. The simulation setup we use is an evolution of that used in Powell et al. (2024) to diagnose the influence of turbulent mixing on the evolution of a passive tracer in the same model flow considered here. The central modification introduced in this work is the two temperature-dependent tracers carried by the plume and the associated parameterisations of moist processes. In § 3 we extend the diagnostic

approach introduced in Powell et al. (2024) to account for the two new 'moist' tracers and the three microphysical processes. To understand tracer transport in stratified flows, it is necessary to consider the evolution of the tracer concentration together with the buoyancy of fluid parcels, since the buoyancy determines the equilibrium position in the stratified environment. We use a 'buoyancy-tracer volume distribution' that maps the flow from physical space to a phase space. Evolution of this distribution is subject to geometric and analytic principles that can be used to identify the influence of turbulent mixing. Having defined the formalism in the context of our idealised model, we review the results presented in Powell et al. (2024) on the evolution of a buoyant plume penetrating into a stably stratified layer and the effect of mixing on a temperature-independent passive tracer. In § 4 we consider a set of simulations where the model parameters that control the influence of the microphysical processes are independently varied to demonstrate the behaviour of our idealised model of convective hydration. We use the diagnostic method introduced in § 3 to describe the TTL 'hydration mechanism' in terms of its simultaneous effect on buoyancy and vapour concentration. This paper is the first of two parts. In Part II, our idealised model is used to investigate the role of sedimentation, mixing, convective intensity, and large-scale vertical shear in convective hydration of a stably stratified layer.

2 | IDEALISED MODEL OF CONVECTIVE HYDRATION

2.1 | Minimal moisture model

We consider the evolution of two moist species: the water vapour concentration $\phi_v(\boldsymbol{x}, t)$ and ice condensate with concentration $\phi_c(\boldsymbol{x}, t)$. The tracer concentrations are dimensionless, with arbitrary units that could be scaled to be representative of quantities such as the mixing ratio. The plume is forced such that only vapour is carried by the plume at the source. Ice is produced via condensation as the plume rises and cools, which reduces the saturation vapour concentration. We assume a fixed sedimentation velocity w_s for ice to aid interpretation of its effect relative to other processes. This is equivalent to assuming a single ice crystal size, which itself determines the sedimentation velocity in more complex microphysical schemes (e.g. Grabowski (1998)). For simplicity, we assume that vapour condenses into ice and ice sublimates into vapour according to the same conversion term $\mathcal{E}$ (but with opposite signs) on the same timescale τ_m. In choosing to model only vapour and ice, we implicitly assume the fast condensation limit, meaning intermediate moist species such as cloud water may be neglected (e.g. Khain et al. (2015); Vallis et al. (2019)). Hence the moist conversion timescale satisfies $\tau_m \ll \tau_d$ where τ_d is the dynamical timescale (defined explicitly later). This limit is representative of deep convection in the tropics; condensation and evaporation occur on timescales of a few seconds to minutes whilst the dynamics occur on the timescale of several minutes (e.g. Rogers and Yau (1989); Hernandez-Duenas et al. (2013)). Upon reaching saturation, any water vapour exceeding the saturation vapour concentration ϕ_{vs} is rapidly converted into ice and when subsaturated, ice (if present) sublimates back into water vapour. This means that supersaturated air is not permitted in our model. Finally, to aid in interpreting results, we include a 'fully passive' tracer ϕ_p with the same forcing as ϕ_v except with no condensation or sublimation processes (i.e. no temperature dependence). In cases with sedimentation, in which ϕ_c does not directly follow the flow so cannot mark the extent of the plume, the fully passive tracer allows consistent definition of 'plume fluid' using a fixed contour $\phi_p \geq 10^{-3}$. The tracer ϕ_p may also be interpreted as the 'total water' in a regime without moist processes, since $\phi_p = \phi_v + \phi_c$ in the absence of sedimentation.

The governing equations for the passive, vapour, and ice tracer concentration are

$$\frac{\mathrm{D}\phi_p}{\mathrm{D}t} = \kappa\nabla^2\phi_p, \tag{1}$$

$$\frac{\mathrm{D}\phi_v}{\mathrm{D}t} = \kappa\nabla^2\phi_v - \mathcal{E}, \tag{2}$$

$$\frac{\mathrm{D}\phi_c}{\mathrm{D}t} - w_s\frac{\partial\phi_c}{\partial z} = \kappa\nabla^2\phi_c + \mathcal{E}, \tag{3}$$

respectively, where κ is the molecular diffusivity (the same for all tracers and buoyancy), w_s is the constant sedimentation velocity (meaning that ϕ_c is conserved) and the moist conversion term $\mathcal{E}$ is given by

$$\mathcal{E} = \frac{\phi_v - \phi_{vs}}{\tau_m}\,\mathcal{H}(\max\{\phi_c, \phi_v - \phi_{vs}\}), \tag{4}$$

where $\mathcal{H}$ is a Heaviside step function. The form of $\mathcal{E}$ is chosen such that condensation occurs when $\phi_v > \phi_{vs}$ and sublimation occurs if $\phi_v < \phi_{vs}$ and $\phi_c > 0$, both on the 'moist conversion' timescale τ_m.

To complete the minimal moisture model we use a representation of the saturation vapour concentration ϕ_{vs}, which depends on temperature T, that is consistent with our Boussinesq numerical scheme (detailed in § 2.3). Following Vallis et al. (2019), assume that the temperature profile is nearly adiabatic, i.e. $\partial_z T \approx -g/c_p$, then $\delta\rho/\rho_0 \approx -\delta\theta/T_0$, where $\delta\theta = \theta - \theta_0$ is the potential temperature perturbation, $\theta_0 = T_0$ is a reference potential temperature (equivalent to the reference absolute temperature T_0) and potential temperature θ is defined as

$$\theta = T + \frac{g}{c_p} z. \tag{5}$$

We use temperature and buoyancy as the key thermodynamic variables. Potential temperature is related to the buoyancy via

$$b = \frac{g}{\theta_0}\delta\theta, \tag{6}$$

and can be derived from the temperature according to (5). The temperature T and buoyancy b are related by

$$T = T_0 + \delta T = T_0 + \frac{T_0}{g} b - \frac{g}{c_p} z. \tag{7}$$

The form of the saturation vapour concentration ϕ_{vs} follows from an approximation to the ideal gas solution of the Clausius-Clapeyron equation, assuming that the latent heat of condensation $\mathcal{L}$ is constant and assuming small variations in absolute and potential temperature (Vallis et al., 2019). We have

$$\phi_{vs} = \phi_0 \exp\left(\alpha \delta T\right), \tag{8}$$

where ϕ_0 is the reference saturation vapour concentration and α is a constant that determines the exponential growth rate of saturation specific humidity with temperature, defined by

$$\alpha = \mathcal{L}/(R_v T_0^2) - c_p/(R_d T_0), \tag{9}$$

where R_v and R_d are the gas constants for water vapour and dry air, respectively.

2.2 | Rescaling

We simulate a scaled-down model flow that is representative of the TTL. Using results presented in Powell et al. (2024) from equivalent simulations to those used here, energy is injected at a $\sim 10^{-1}$ m scale and dissipated at the Kolmogorov scale $\eta_k \sim 10^{-5}$ m with a resolved grid scale $\sim 10^{-3}$ m. In atmospheric convection (Feist et al., 2019), energy is injected at a $\sim 10^4$ m scale and dissipated at the Kolmogorov scale $\eta_k \sim 10^{-3}$ m with a resolved grid scale $\sim 10^2$ m. Thus a larger fraction of the inertial subrange is resolved in the simulations presented in this paper compared with previous studies.

In order to represent moist processes in the TTL realistically, all variables and constants must be converted from geophysical scales to the simulated scale. We choose characteristic time and length scales relevant to the TTL and the corresponding values in our simulation setup to form scale factors for each quantity. This is equivalent to first non-dimensionalising the system and then re-dimensionalising for a given scale. For the characteristic lengthscale, we choose the depth of the uniform layer $H = 0.2$ m which corresponds with the depth of the troposphere $H_{\text{atm}} = 14$ km, giving a length scale factor $R_l = H_{\text{atm}}/H = 7 \times 10^4$. Note that choosing a horizontal lengthscale, such as the plume radius at penetration, may be more appropriate given its direct influence on transport into the stratified layer. However, it is difficult to calculate the corresponding scale in the TTL since overshoots vary significantly in width (Dauhut et al., 2018) and the choice between the radius of the entire overshoot complex or the central updraft is ambiguous. For the timescale we choose the time taken for a convective overshoot to penetrate, collapse and settle, τ_p. From Dauhut et al. (2018) we estimate $\tau_{p,\text{atm}} \approx 10$ min. in the TTL, corresponding to $\tau_{p,\text{sim}} \approx 15$ s with the simulation setup described in § 2.3, giving a time scale factor $R_t = \tau_{p,\text{atm}}/\tau_{p,\text{sim}} = 40$. Under this scaling, a typical value of the stratification strength in the TTL $N^2_{\text{atm}} \approx 6 \times 10^{-4}\ \text{s}^{-2}$ translates to $N_0^2 \approx 0.96\, s^{-2}$ in our simulations. These conversions are summarised in table 1. Henceforth all values and figures are presented in the geophysical scale unless otherwise stated.

There is no natural choice for the temperature scaling in our simulations, so we continue to use temperature values corresponding to a choice of reference temperature $T_0 = 300$ K. With b and z at the simulation scale, the temperature in our model is

$$T = T_0 + \Theta b - \Gamma(z + H), \tag{10}$$

Quantity	Simulation value	Geophysical equivalent	Conversion factor
Uniform layer depth H	0.2 m	14 km	$R_l = 7 \times 10^4$
Overshoot timescale τ_p	15 s	10 min.	$R_t = 40$
Stratification N_0^2	0.96 (s^{-2})	6×10^{-4} (s^{-2})	R_t^{-2}

TABLE 1 Conversion between characteristic quantities in the TTL and our simulations.

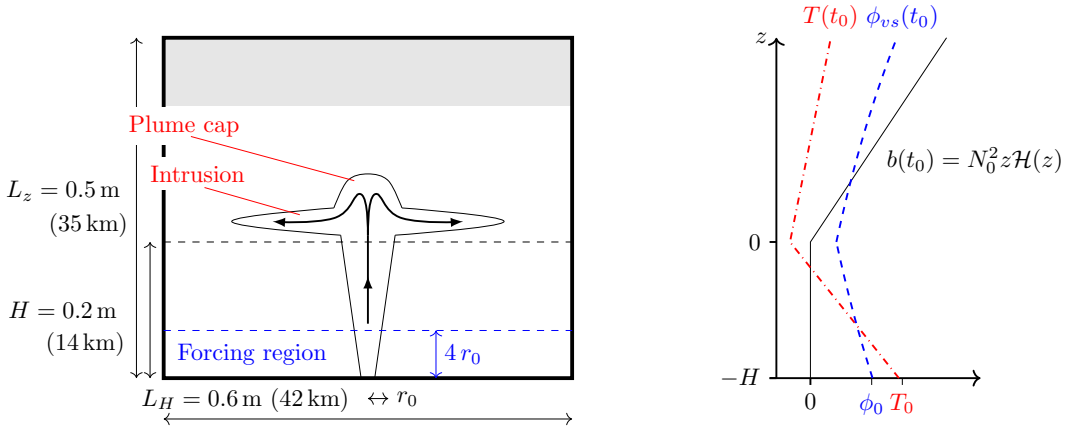

FIGURE 1 Schematic of simulation setup (left) and initial buoyancy $b(t_0)$, temperature $T(t_0)$ and saturation vapour concentration $\phi_{vs}(t_0)$ profiles (right). The plume cap and intrusion are labelled in red. The forcing region is labelled in blue, where the plume forcing terms f_w, f_b, f_{ϕ_p}, and f_{ϕ_v} in (19)–(22) are non-zero. The simulation domain lengths L_z, L_H, plume source radius r_0, and uniform layer depth H are as defined in the schematic (equivalent geophysical scales shown in brackets) and given in table 2.

where $\Theta = T_0 R_l/(gR_t^2)$ is the conversion between buoyancy and potential temperature perturbation, such that $\delta\theta = \Theta b$, and $\Gamma = gR_l/c_p$ is the 'dry adiabatic' lapse rate in our model. This provides a mechanism for (an analogue to) 'adiabatic cooling' and 'adiabatic warming' in our model, where fluid is cooled (warmed) as it moves upwards (downwards), which in turn reduces (increases) ϕ_{vs}. The saturation vapour concentration is then

$$\phi_{vs} = \phi_0 \exp\left[\alpha(T - T_0)\right] = \phi_0 \exp\left[\alpha\left(\Theta b - \Gamma(z + H)\right)\right], \tag{11}$$

where α is a constant defined in (9) that depends on other physical constants and ϕ_0 is the reference saturation concentration, a free parameter that can be set along with the plume forcing $F_0^{(\phi)}$ to determine how much condensation occurs (see §2.4). Note that by neglecting latent heating, the moist static energy is directly equivalent to the buoyancy b. The dry and saturated adiabatic lapse rates are also identical and no buoyancy or vapour sources or sinks are present in the domain except for the forcing region where the plume is generated.

2.3 | Numerical implementation & simulation setup

The simulation setup and numerical scheme is identical to that detailed in Powell et al. (2024) except with minor modifications to the tracer initial conditions, the introduction of vertical shear in the stratified layer (for consideration in Part II), and an additional factor in the plume forcing terms that switches off plume forcing at time t_{lim}. Here, we briefly summarise the simulation setup and refer the reader to Powell et al. (2024) for full details.

We consider the penetration of a buoyant plume with source radius r_0 and source integral buoyancy flux F_0 generated in a uniform layer of depth $H = 0.2$ m into a stable linearly stratified layer with buoyancy frequency $N_0 = 1.0\,\mathrm{s}^{-1}$. The bottom of the (initial) stratified layer is defined as $z = 0$ and we define $t = 0$ as the time at which the plume first penetrates into the stratified

layer. The 3D computational domain has width $L_h = 0.6\,\mathrm{m}$ and height $L_z = 0.6\,\mathrm{m}$. The initial conditions are

$$\boldsymbol{u}(\boldsymbol{x}, t_0) = \begin{cases} \boldsymbol{0} & -H \le z \le 0, \\ \lambda z \hat{\boldsymbol{x}} & 0 \le z \le L_z - H, \end{cases} \tag{12}$$

$$b(\boldsymbol{x}, t_0) = \begin{cases} 0 & -H \le z \le 0, \\ N_0^2 z & 0 \le z \le L_z - H, \end{cases} \tag{13}$$

$$\phi_{p,v,c}(\boldsymbol{x}, t_0) = \mathcal{N}, \tag{14}$$

where $\lambda = \partial_z u$ is the vertical shear rate in the stratified layer (set to zero in this paper; the role of vertical shear is explored in Part II) and $\mathcal{N}$ represents random noise of magnitude 10^{-8} applied independently to all tracers. The noise is included to handle a numerical instability in the SGS diffusivity calculation. Note that the domain is chosen to be initially completely dry.

From (13), the initial conditions for the temperature T are

$$T(\boldsymbol{x}, t_0) = \begin{cases} T_0 - \Gamma(z + H) & -H \le z \le 0, \\ T_0 + (\Theta N_0^2 - \Gamma) z - \Gamma H & 0 \le z \le L_z - H, \end{cases} \tag{15}$$

Note that with the intention to use this model to explore processes in the TTL, where temperatures increase with height above the CPT (corresponding to $z = 0$), we are restricted to $\Theta N_0^2 > \Gamma$ so that $\partial_z T > 0$ in the stratified layer. The boundary conditions on the top and bottom boundaries are no-slip $\partial_z u = \partial_z v = 0$, no-penetration $w = 0$ and no-flux $\partial_z b = \partial_z \phi = 0$. Figure 1 shows a schematic of the simulation setup and illustrative initial profiles of the temperature, saturation vapour concentration, and buoyancy. The simulation dimensions are shown with geophysical equivalent dimensions in brackets. The key structures of the plume referred to throughout this paper are labelled in red.

We generate the buoyant plume by forcing the vertical velocity w, buoyancy b, passive and vapour tracer concentrations ϕ_p and ϕ_v in the shallow forcing region of depth L_c indicated in figure 1. In this region, the variables are relaxed towards prescribed profiles that describe the 'pure' plume solutions of the Morton et al. (1956) axisymmetric plume equations for a given source radius r_0, integral source buoyancy flux F_0, and integral source tracer flux $F_0^{(\phi)}$ which (at the simulated scale) is identical for the passive and vapour tracer concentrations. A 'pure' plume is forced such that the buoyancy and momentum fluxes are balanced at the source, so only the buoyancy flux is needed to determine the strength of the plume. The plume centreline lies at the middle of the computational domain, $x_p = y_p = L_h/2$. The integral source fluxes are defined as

$$F_0 = 2 \int_0^\infty \overline{wb}\big|_{z=-H} \, r \, \mathrm{d}r, \tag{16}$$

$$F_0^{(\phi)} = 2 \int_0^\infty \overline{w\phi_p}\big|_{z=-H} \, r \, \mathrm{d}r \approx 2 \int_0^\infty \overline{w\phi_v}\big|_{z=-H} \, r \, \mathrm{d}r, \tag{17}$$

where $\bar{\cdot}$ denotes an azimuthal and time average. Turbulence is initiated in the plume by applying a 10% perturbation to the forcing profiles in the forcing region and to all velocity components in the two grid layers above the forcing region.

The numerical scheme evolves the Boussinesq Navier-Stokes equations with the anisotropic minimum dissipation (AMD) eddy-viscosity model to represent unresolved scales (Vreugdenhil and Taylor, 2018). For consistency with Powell et al. (2024), we state the full governing for velocity $\boldsymbol{u}$ and scalars b, ϕ_p, ϕ_v, and ϕ_c non-dimensionalised by F_0 and N_0,

$$\nabla \cdot \widehat{\boldsymbol{u}} = 0, \tag{18}$$

$$\frac{\mathrm{D}\widehat{\boldsymbol{u}}}{\mathrm{D}t} + \nabla \widehat{p} = \frac{1}{\mathrm{Re}} \nabla^2 \widehat{\boldsymbol{u}} + \widehat{b}\hat{\boldsymbol{k}} - \nabla \cdot \boldsymbol{\tau} + f_w \hat{\boldsymbol{k}}, \tag{19}$$

$$\frac{\mathrm{D}\widehat{b}}{\mathrm{D}t} = \frac{1}{\mathrm{Re}\,\mathrm{Pr}} \nabla^2 \widehat{b} - \nabla \cdot \boldsymbol{\lambda}_b + f_b, \tag{20}$$

$$\frac{\mathrm{D}\widehat{\phi}_p}{\mathrm{D}t} = \frac{1}{\mathrm{Re}\,\mathrm{Pr}} \nabla^2 \widehat{\phi}_p - \nabla \cdot \boldsymbol{\lambda}_{\phi_p} + f_{\phi_p}, \tag{21}$$

$$\frac{\mathrm{D}\widehat{\phi}_v}{\mathrm{D}t} = \frac{1}{\mathrm{Re}\,\mathrm{Pr}} \nabla^2 \widehat{\phi}_v - \nabla \cdot \boldsymbol{\lambda}_{\phi_v} - \widehat{\mathcal{E}} + f_{\phi_v}, \tag{22}$$

$$\frac{\mathrm{D}\widehat{\phi}_c}{\mathrm{D}t} = \frac{1}{\mathrm{Re}\,\mathrm{Pr}} \nabla^2 \widehat{\phi}_c - \nabla \cdot \boldsymbol{\lambda}_{\phi_c} + \widehat{\mathcal{E}} + w_s \frac{\partial \widehat{\phi}_c}{\partial z}, \tag{23}$$

Parameter	Definition / Use	Description	Simulation value	Geophysical equivalent
T_0	(7)	Reference temperature	300 K	300 K
w_s	(3)	Sedimentation velocity of ice	Varied	
τ_m	(4)	Moist conversion timescale	0.1 s	4 s
ϕ_0	(11)	Reference saturation concentration	Varied in Part I, 0.2 in Part II	
α	(9)	ϕ_{vs} exponential growth rate	0.05 K^{-1}	0.05 K^{-1}
Θ	(10)	$\delta\theta = \Theta b$	1340 $K^{-1}/(m\ s^{-2})$	30.63 $K^{-1}/(m\ s^{-2})$
Γ	(10)	Dry adiabatic lapse rate	684 K m^{-1}	9.77 K km^{-1}
λ	(12)	Vertical shear rate in stratified layer	0 s^{-1}	0 s^{-1}
L_h, L_z	Fig 1	Domain width & height	0.6, 0.5 m	42, 35 km
F_0	(16)	Source buoyancy flux	6×10^{-8} $m^4\ s^{-3}$	2.3×10^7 $m^4\ s^{-3}$
$F_0^{(\phi)}$	(17)	Source passive & vapour tracer flux	6×10^{-8} $m^3\ s^{-1}$	5.1×10^5 $m^3\ s^{-3}$
N_0	(13)	Stratified layer buoyancy frequency	1.0 s^{-1}	2.5×10^{-2} s^{-1}
H	Fig 1	Uniform layer depth	0.2 m	14 km
r_0	Fig 1	Source plume radius	0.002 m	140 m
t_{end}		Simulation end time	15 s	10 min.
τ_r	(24)	Limited forcing relaxation timescale	0.5 s	20 s
t_{lim}	(24)	Plume forcing end time	10 s	6⅔ min.

TABLE 2 Minimal moisture model parameters and general simulation parameters with values given for parameters fixed in all simulations. Equivalent geophysical scales shown where appropriate.

where $\widehat{\cdot}$ indicates filtering at the resolved grid scale, $\hat{\boldsymbol{k}}$ is the unit vector in the vertical direction, and the plume forcing terms f_w,f_b,f_{ϕ_p}, and f_{ϕ_v} are defined as in appendix A of Powell et al. (2024) except with the tracer ϕ replaced by ϕ_p and ϕ_v in the natural way. These terms generate the plume in the forcing region at the bottom of the domain as indicated in figure 1, by relaxing the vertical velocity, buoyancy, and tracers towards analytic profiles for a pure plume, i.e. Gaussian radial profiles with a characteristic radius that linearly increases with height (Morton et al., 1956). An additional multiplicative factor

$$f_t(t) = \frac{1}{2}\left[1 - \tanh\left(\frac{t - t_{\text{lim}}}{\tau_r}\right)\right], \tag{24}$$

is included which ends plume forcing at time $t \approx t_{\text{lim}}$ over a relaxation timescale τ_r. The two dimensionless parameters are the Reynolds number and Prandtl number,

$$\text{Re} = \frac{F_0^{1/2}}{\nu N_0^{1/2}}, \quad \text{Pr} = \frac{\nu}{\kappa}, \tag{25}$$

where ν is the molecular viscosity. The SGS stress tensor $\boldsymbol{\tau}$ has components $\tau_{ij} = \widehat{u_i u_j} - \widehat{u}_i\widehat{u}_j$, the SGS buoyancy flux is $\boldsymbol{\lambda} = \widehat{\boldsymbol{u}b} - \widehat{\boldsymbol{u}}\widehat{b}$ and the SGS tracer fluxes are $\boldsymbol{\lambda}_{\phi_i} = \widehat{\boldsymbol{u}\phi_i} - \widehat{\boldsymbol{u}}\widehat{\phi}_i$. Finally, $\widehat{\mathcal{E}}$ is the moist conversion term defined in (4) with ϕ_v and ϕ_c replaced by the filtered variables $\widehat{\phi}_v$ and $\widehat{\phi}_c$. To avoid confusion when varying F_0, we drop the non-dimensionalisation henceforth. Simulation parameters are summarised in table 2. Values are given for fixed parameters.

The random noise in (14) required for stability of the SGS diffusivity calculation introduces a complication in the numerical implementation. The form of the condensation/sublimation term in (22) and (23) means that ϕ_c and ϕ_p are modified when $\phi_v > \phi_{vs}$ or when $\phi_v < \phi_{vs}$ and $\phi_c > 0$. Given a time step Δt, from (22) the change in ϕ_v is approximately

$$\left|\Delta\phi_v\right| \approx \left|\phi_v - \phi_{vs}\right| \frac{\Delta t}{\tau_m}, \tag{26}$$

and similarly for ϕ_c. At the top of the domain, this introduces a numerical instability since ϕ_v is non-zero and small due to the imposed noise but ϕ_{vs} is extremely large, so $\Delta\phi_v$ far exceeds the amount of ice available to sublimate unless the time step Δt is restricted to being very small. To avoid excessive constraints on the time step without allowing 'too much' sublimation to occur, we explicitly check when $\Delta\phi_v > \phi_c$ and instead set $\Delta\phi_v = \phi_c$ so that $\phi_v \mapsto \phi_v + \phi_c$ and $\phi_c \mapsto 0$.

For consistency with the fast condensation limit, the moist conversion timescale τ_m is chosen to be smaller than the dynamical timescale τ_d that could be defined in various ways; here we choose the time taken for fluid parcels to rise from penetration to the top of the plume, which scales with N_0^{-1} (Devenish et al., 2010). This is approximated as the ratio of the quasi-steady state height of the plume z_{ss} and the time- and azimuthal-average vertical velocity on the plume centreline $\boldsymbol{x}_p = (L_h/2, L_h/2, 0)$ at penetration:

$$\tau_d = \frac{z_{\text{ss}}}{\overline{w}(\boldsymbol{x}_p)}. \tag{27}$$

On average, the simulations presented here and in Part II have $\tau_m/\tau_d \approx 0.05$.

We use DIABLO (Taylor, 2008) to perform three-dimensional LES of the setup shown in figure 1. DIABLO evolves the Boussinesq Navier-Stokes equations (18) – (23) discretised using Fourier modes in the two periodic horizontal directions and second-order finite differences in the vertical direction. The boundary conditions on the top and bottom boundaries are no-slip and no-penetration. A third-order Runge-Kutta scheme is used for time-stepping. A 2/3 dealiasing rule is applied when transforming from Fourier to physical space. We use a uniform grid of $512^2 \times 513$ points. In the top 20% of the domain, a sponge layer damps the velocity towards zero and the buoyancy towards the initial stratification $b(t_0)$ to inhibit the reflection of internal gravity waves from the top boundary. Validation of the numerical method is detailed in appendix B of Powell et al. (2024).

2.4 | Quantifying model regimes

Here, we introduce dimensionless 'regime numbers' $R_\mathrm{H}, R_\mathrm{S}$, and R_SH, which quantify the importance of phase change, sedimentation, and large-scale vertical shear, respectively, relative to characteristic plume quantities. These regime numbers are fixed in each simulation.

For our focus on the transport of water vapour into the stratified layer, it is important to quantify the extent to which condensation of vapour into ice occurs as the plume rises through the uniform layer, since this sets the partitioning of moisture into vapour and ice at penetration. We use a 'conserved' relative humidity

$$R_\mathrm{H} = \frac{\overline{\phi}_p(\boldsymbol{x}_p)}{\phi_0 \exp\left[\alpha\left(\overline{b}(\boldsymbol{x}_p) - \beta H\right)\right]}, \tag{28}$$

which is the ratio of the time- and azimuthally-averaged passive tracer $\overline{\phi_p}$ and the saturation vapour concentration $\overline{\phi_{vs}}$ on the plume centreline at penetration $\boldsymbol{x}_p = (L_h/2, L_h/2, 0)$. The time average is taken over the period $0 \leq t \leq t_\mathrm{lim}$ where the plume remains forced after penetration. The dimensionless number R_H can be interpreted as the mean relative humidity on the plume centreline at penetration assuming condensation does not occur. When R_H exceeds unity, the vapour concentration – if it were conserved – would exceed the saturation concentration at penetration so condensation must have occurred in the uniform layer. Similarly, when $R_\mathrm{H} \gg 1$ then extensive condensation occurs as the plume rises through the uniform layer, so the plume is 'ice-loaded' at penetration. Conversely, when $R_\mathrm{H} \ll 1$ then the plume penetrates carrying very little ice. The large R_H regime is the atmospherically interesting case, as shown by observational evidence (Khaykin et al., 2009) and numerical simulations, e.g. Dauhut et al. (2018) – their figure 7(d) shows the solid water (i.e. ice) mixing ratio around 10^4 ppmv and the vapour mixing ratio around 10 ppmv at the height of the CPT in an overshoot that produces a net hydration above the 380 K isentrope (used to define stratospheric air). Translating to the language of our model, and assuming that sedimentation is weak (which is valid in the central updraft, see later), then $\phi_p = \phi_v + \phi_c \approx 10^4$ at penetration and hence $R_\mathrm{H} \approx 10^3$. The regime number R_H is controlled by two parameters: the plume buoyancy and tracer fluxes F_0 and $F_0^{(\phi)}$, which modify b, ϕ_p, and ϕ_v in the plume, and the reference saturation vapour concentration ϕ_0, which varies the environmental saturation profile and thus modifies the amount of vapour needed to reach saturation. When F_0 or $F_0^{(\phi)}$ is large, the pseudo-spectral numerical method is susceptible to unphysical oscillations known as 'Gibbs ringing' (see Gelb and Gottlieb (2007) or DeBonis (2019) for a review of the phenomenon and appendix B of Powell et al. (2024) for assessment of its (negligible) effect on our simulations). These oscillations arise as a result of large changes in the values of the buoyancy or tracers over a short distance (i.e. one or two grid cells) from within to outside the plume, particularly lower in the domain where the plume radius is small. As a result, the choice of $F_0^{(\phi)}$ and F_0 is limited so we cannot explore regimes where R_H is extremely large, which require large values of ϕ_p within the plume. Test simulations showed that $R_\mathrm{H} \approx 15$ is the practical limit with our numerical setup.

The importance of sedimentation is expressed by a dimensionless number

$$R_\mathrm{S} = \frac{w_s}{w_\mathrm{eddy}}, \tag{29}$$

which is the ratio of the sedimentation velocity w_s and the mean turbulent vertical velocity in the plume,

$$w_\mathrm{eddy} = \langle w' \rangle^\mathrm{plume}, \tag{30}$$

where $\langle\cdot\rangle^\mathrm{plume}$ indicates the plume average where $\phi_p \geq 10^{-3}$ within the stratified layer $z \geq -L$, averaged over the time range $0 \leq t \leq t_\mathrm{lim}$ where plume forcing is active. The turbulent component of the vertical velocity, w', is calculated by subtracting

the running mean of the azimuthally averaged velocity. Here, the running mean is taken over a time period of 25 'turnover times' $T_{\{F_0,r_0\}} = r_0^{4/3}F_0^{-1/3}$, interpreted as the time for an eddy to become significantly distorted (Frisch, 1995), which smooths out eddy fluctuations. When $R_S \gg 1$ the turbulent vertical velocity within the plume is significantly weaker than the sedimentation velocity and we expect that ice falls out of suspension and therefore does not reach as far into the stratified layer. When $R_S \ll 1$ the sedimentation velocity is weak relative to turbulent eddies in the plume and therefore sedimentation plays little role in the dynamics.

Finally, the strength of the vertical shear in the horizontal velocity in the environment, relative to plume velocities, is quantified by the dimensionless number

$$R_{SH} = \frac{\tau_d}{\lambda^{-1}} \tag{31}$$

which is the ratio of the dynamical timescale τ_d and the shear timescale λ^{-1}, where $\lambda = \partial_z u$ as defined in (12). Thus when $R_{SH} \gg 1$ the shear timescale is much shorter than the timescale of the dynamics so shear effects are strong and the plume cap becomes significantly distorted by the large-scale horizontal flow in the stratified layer. When $R_{SH} \ll 1$ the shear plays little role in the dynamics.

3 | MOIST BUOYANCY-TRACER VOLUME DISTRIBUTION

3.1 | Definitions

In stratified flows, mixing must be assessed both in terms of the (moist) tracer concentration and the buoyancy, since the buoyancy determines the neutral height of a fluid parcel and consequently its position once the flow restratifies. In our model the buoyancy also directly influences the tracer concentrations by placing an upper limit $\phi_{vs}(T)$ on the vapour concentration via the temperature T. To explore the combined effect of moist processes and mixing, we extend the buoyancy-tracer volume distribution formalism introduced in Powell et al. (2024) which maps the flow from physical space to a 2D phase space with the buoyancy and tracer concentration as coordinates. At each point in this phase space, the volume distribution W represents the volume of fluid in physical space (within a specified control volume, here the stratified layer) with the given value of buoyancy and tracer concentration. Formally, for a given tracer ϕ_i with $i = v, c, p$ the volume distribution W_i is defined as

$$W_i(B, \Phi; t) = \int_V \delta(b(\boldsymbol{x}, t) - B)\delta(\phi_i(\boldsymbol{x}, t) - \Phi)\,\mathrm{d}V, \tag{32}$$

where δ is the Dirac delta function, V is the control volume, and B and Φ are dummy coordinates in the corresponding buoyancy-tracer phase space. The governing equations for the distributions are

$$\frac{\partial W_p}{\partial t} = -S_p - \nabla_p \cdot \boldsymbol{F}_p, \tag{33}$$

$$\frac{\partial W_v}{\partial t} = -S_v - \nabla_v \cdot \boldsymbol{F}_v - \frac{\partial J_v}{\partial \phi_v}, \tag{34}$$

$$\frac{\partial W_c}{\partial t} = -S_c - \nabla_c \cdot \boldsymbol{F}_c - \frac{\partial J_c}{\partial \phi_c} - \frac{\partial K}{\partial \phi_c}, \tag{35}$$

where $\nabla_i = (\partial_b, \partial_{\phi_i})$ is the gradient in (b, ϕ_i)-space for $i = p, v, c$. The source distributions S_i and mixing flux distribution $\boldsymbol{F}_i$ for each tracer ϕ_i are defined as

$$S_i(B, \Phi; t) = \int_{\partial V} \boldsymbol{u} \cdot \boldsymbol{n}\, \delta(b(\boldsymbol{x}, t) - B)\delta(\phi_i(\boldsymbol{x}, t) - \Phi)\,\mathrm{d}A, \tag{36}$$

$$\boldsymbol{F}_i(B, \Phi; t) = \int_V (\dot{b}, \dot{\phi}_i)\, \delta(b(\boldsymbol{x}, t) - B)\delta(\phi_i(\boldsymbol{x}, t) - \Phi)\,\mathrm{d}V, \tag{37}$$

where $\dot{b} = \kappa\nabla^2 b - \nabla\cdot\boldsymbol{\lambda}_b$ and $\dot{\phi}_i = \kappa\nabla^2\phi_i - \nabla\cdot\boldsymbol{\lambda}_{\phi_i}$ represent the effect of diffusive mixing on b and ϕ_i. The additional 'moist' terms in (34) and (35) are

$$J_v(B,\Phi;t) = -\int_V \left[\frac{\phi_v-\phi_{vs}}{\tau_m}\,\mathcal{H}(\max\{\phi_c,\phi_v-\phi_{vs}\})\right]\delta(b(\boldsymbol{x},t)-B)\,\delta(\phi_v(\boldsymbol{x},t)-\Phi)\,\mathrm{d}V, \tag{38}$$

$$J_c(B,\Phi;t) = \int_V \left[\frac{\phi_v-\phi_{vs}}{\tau_m}\,\mathcal{H}(\max\{\phi_c,\phi_v-\phi_{vs}\})\right]\delta(b(\boldsymbol{x},t)-B)\,\delta(\phi_c(\boldsymbol{x},t)-\Phi)\,\mathrm{d}V, \tag{39}$$

$$K(B,\Phi;t) = \int_V \left[w_s\frac{\partial\phi_c}{\partial z}\right]\delta(b(\boldsymbol{x},t)-B)\,\delta(\phi_c(\boldsymbol{x},t)-\Phi)\,\mathrm{d}V, \tag{40}$$

which are referred to as the vapour condensation flux, ice sublimation flux, and sedimentation flux respectively. To summarise, the volume distribution W_v represents the amount of fluid in the plume within the stratified layer with buoyancy and vapour concentration within a given range. Mixing acts to move volume through (b,ϕ_v)-space (modifying W_v) which is captured by the mixing flux $\boldsymbol{F}_v$, and the movement of volume due to changes in the vapour concentration via condensation are represented by J_v. The source distribution S_v captures plume fluid entering the stratified layer. The conversion of moist tracers between vapour and ice and sedimentation of ice is represented by the terms J_v, J_c and K which could be interpreted as vectors in (b,ϕ_v)-space (for J_v) or (b,ϕ_c)-space (for J_c and K) with no component in the b direction, representing the fact that moist conversion and sedimentation acts on the tracer concentration(s) alone, with no effect on the buoyancy of fluid parcels. The governing equations and constituent terms can be derived following appendix C of Powell et al. (2024), replacing the tracer governing equation with (21)–(23). Note that (38)–(40) are written as functions of (B,Φ) to aid clarity and for consistency with definitions given in Powell et al. (2024) but henceforth all 'vapour' distributions (with a subscript v) are written as functions of b and ϕ_v and similarly for the 'ice' and 'passive' distributions.

The numerical implementation of these distributions is as described in detail in Powell et al. (2024). In summary, the distributions are calculated by discretising buoyancy in the range $b_{\min} < b < b_{\max}$ into N_b equispaced bins. Similarly, each tracer concentrations ϕ_i is discretised into N_{ϕ_i} equispaced bins in the range $\phi_{\min} < \phi_i < \phi_{\max}$. We use $N_b = N_\phi = 256$. The minimum buoyancy is set to $b_{\min} = 0$ so that only fluid with non-zero buoyancy (i.e. in the stratified layer) is represented in the distribution. The minimum vapour, ice and passive tracer concentrations $\phi_{v,\min}$, $\phi_{c,\min}$ and $\phi_{p,\min}$ are chosen so that Gibbs ringing artefacts (which can produce small, non-zero values of the tracer concentration) are excluded from the distribution. In some cases, particularly when $R_{\mathrm{H}} \gg 1$, the minimum saturation concentration can fall below $\phi_{v,\min}$. However, this issue applies to relatively few fluid parcels in the domain and does not qualitatively affect the results. In simulations presented here and in Part II we use $\phi_{v,\min} = \phi_{c,\min} = \phi_{p,\min} = 2\times10^{-4}$. We define the 'stratified layer' (where the volume distribution is computed) to be $z \geq -L$ where $L = F_0^{1/4}N_0^{-3/4}$ is the characteristic length scale when non-dimensionalising with F_0 and N_0. This accounts for the slight deformation of the bottom of the stratified layer below its initial height $z = 0$ as the plume intrusion spreads laterally.

3.2 | Evolution of the passive volume distribution

To act as a summary of the dynamics that will be seen in the simulations and to illustrate use of the buoyancy-tracer volume distribution formalism, here we review the transport and mixing of a temperature-independent 'fully passive' tracer in convective penetration of a stratified layer with no parameterisation of moist processes, as detailed in Powell et al. (2024). The volume distribution W_p has a 'convex envelope' property: in the case we consider where the diffusivity of the buoyancy and tracer is identical, the mixture of a set of fluid parcels in buoyancy-tracer space lies within the convex envelope of the original set of fluid parcels (Penney et al., 2020). We can therefore understand mixing in the flow by building a geometric picture of the correspondence between buoyancy-tracer and physical space and identifying regions which are mixing in buoyancy-tracer space using the mixing flux distribution $\boldsymbol{F}_p$. Details of this analysis are given in Powell et al. (2024); here we focus on describing the evolution of the volume distribution W_p and relate this evolution to the dynamics of convective penetration.

In the flow we consider, plume fluid parcels carrying passive tracer lie on a line in buoyancy-tracer space because, in a turbulent pure plume, the radial profiles of buoyancy and tracer concentration are, on average, Gaussian with the same characteristic width – hence $b \propto \phi_p$. We refer to this line in buoyancy-tracer space as the 'source line'. Environmental fluid with a range of buoyancy but zero tracer concentration lies on the buoyancy axis $\phi_p = 0$ in buoyancy-tracer space. Mixing between the plume and environment acts to mix together fluid parcels on the source line and parts of the buoyancy axis which are 'accessible' in the sense that the plume has reached the corresponding height in the stratification and can therefore mix with environmental fluid of

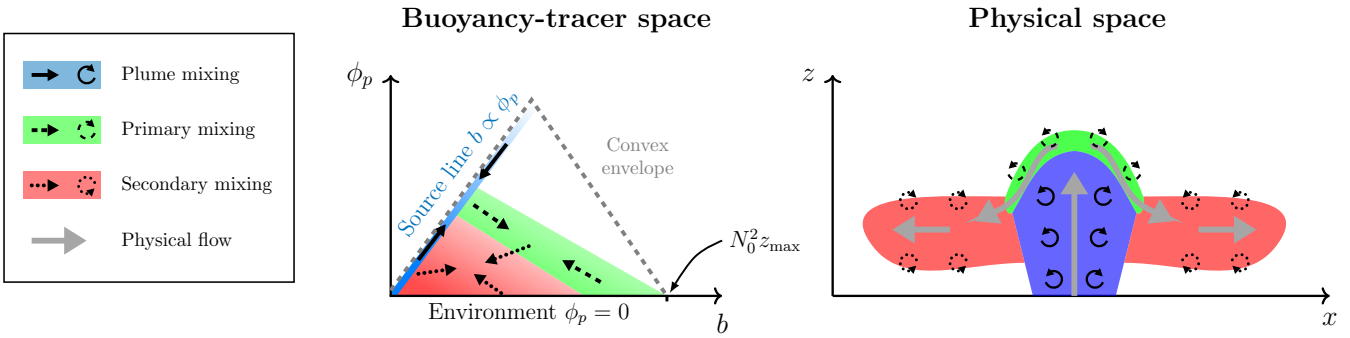

FIGURE 2 Schematic illustration of the evolution of the passive buoyancy-tracer volume distribution in convective penetration of a stably stratified layer in buoyancy-tracer space (left) and the corresponding flow in physical space (right). Black (circular) arrows indicate approximate location of mixing (in physical space) and effect on volume distribution (in buoyancy-tracer space). Coloured regions and line styles indicate the mixing stage: solid - plume mixing in the undiluted rising plume (blue), dashed - primary mixing in the plume cap (green), dotted - secondary mixing in the intrusion (red). The flow in physical space is indicated by grey arrows (right). In buoyancy-tracer space, the convex envelope of the initial volume distribution (i.e. the source line and accessible range of the buoyancy axis) is indicated by the grey dashed line (left).

Regime	R_H	R_S	ϕ_0	Simulation w_s (m s^{-1})	Geophysical equivalent w_s (m s^{-1})
$R_H \gg 1$	8.54	0	0.2	0	0
$R_H \sim 1$	0.89	0	2.0	0	0
$R_H \ll 1$	0.10	0	15	0	0
$R_S \gg 1$	2.49	6.45	0.5	5×10^{-2}	87.5
$R_S \sim 1$	2.09	0.66	0.5	5×10^{-3}	8.75
$R_S \ll 1$	2.15	0.01	0.5	5×10^{-5}	8.75×10^{-2}

TABLE 3 Simulation parameters for the regime-exploring simulations presented in § 4. Remaining parameters are as given in table 2 and in the text.

that buoyancy. A reasonable approximation for the maximum accessible buoyancy is $b = N_0^2 z_{\max}$, determined by the maximum penetration height, $z_{\max}$, measured from the bottom of the stratified layer $z = 0$ (Powell et al., 2024).

To understand the evolution of W_p it remains to describe the flow of volume through the convex envelope of the source line and the buoyancy axis $0 \leq b \leq N_0^2 z_{\max}$. Figure 2 shows a schematic of the flow evolution in (passive) buoyancy-tracer space and physical space. This evolution consists of three stages of mixing.

1. Plume mixing occurs as plume fluid rises into the stratified layer, acting to mix fluid on the plume centreline, where b and ϕ_p are largest, with fluid on the plume edge where b and ϕ_p are smaller (solid arrows in figure 2). At this stage, plume fluid is shielded from the surrounding environment by the intrusion so no mixing between the plume and environment occurs and plume fluid remains undiluted. In buoyancy-tracer space, this means mixing only occurs within the blue region in figure 2 and acts to homogenise undiluted plume fluid, moving volume towards the centre of the source line.
2. Primary mixing occurs once plume fluid is exposed to the environment at the edge of the plume cap near $z_{\max}$. Mixing occurs within the green region in buoyancy-tracer space in figure 2 between undiluted plume fluid at the centre of the source line and the most buoyant environmental fluid accessible to the plume (dashed arrows in figure 2). Newly-formed mixtures of plume and environmental fluid subside from the plume cap and join the intrusion.
3. Secondary mixing occurs as mixed fluid joins the radially-spreading intrusion. Further entrainment of environmental fluid occurs as the plume spreads radially (dotted arrows in figure 2). Some fluid parcels move directly from the undiluted rising plume into the intrusion (moving directly from the source line to the red region in buoyancy-tracer space in figure 2). As mixed fluid becomes homogenised in the intrusion, volume accumulates in a small region of buoyancy-tracer space.

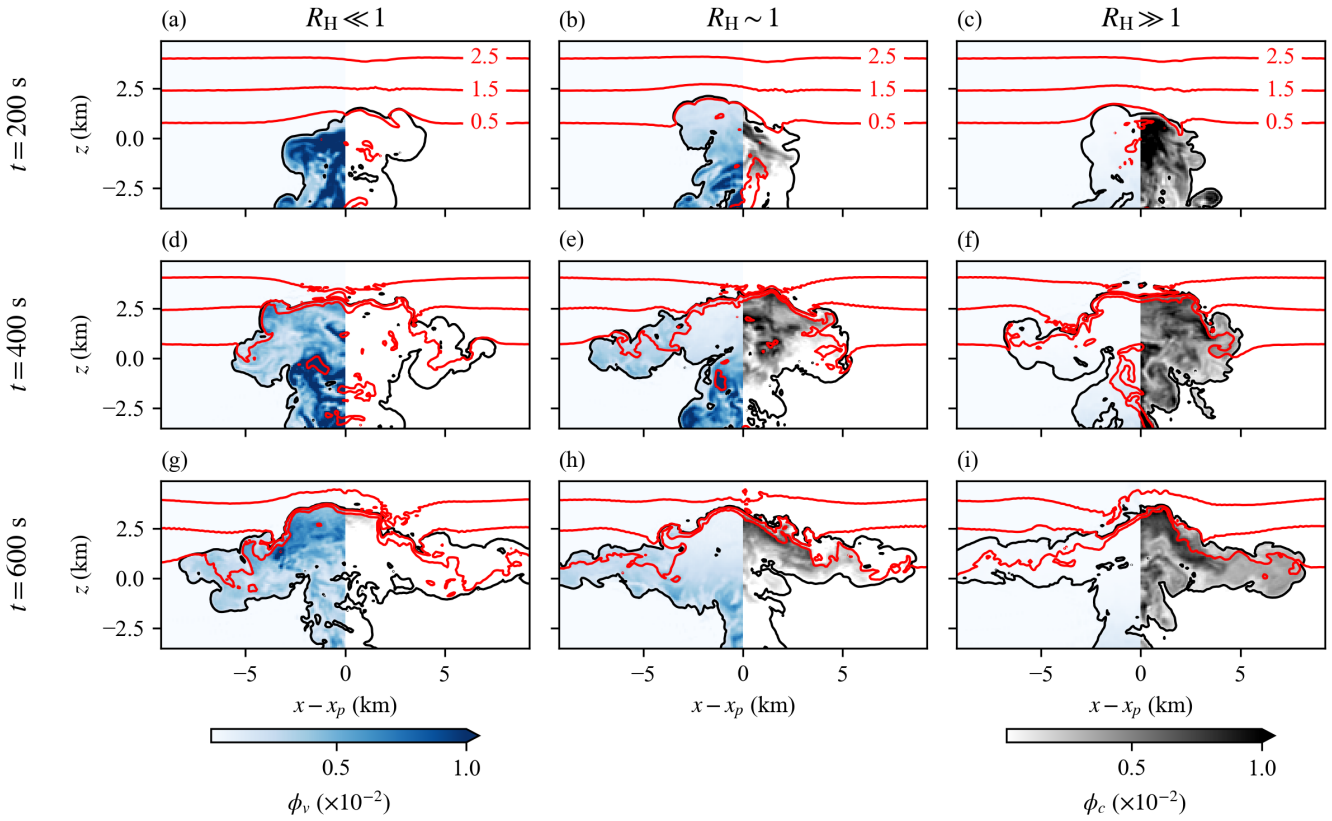

FIGURE 3 Snapshots of simulations with varied ϕ_0 and $w_s = 0$ at $t = (\frac{1}{3}, \frac{2}{3}, 1)\, t_{\text{end}}$, showing the vapour concentration ϕ_v and ice concentration ϕ_c in each panel. These simulations are representative of regimes with $R_H \ll 1, R_H \sim 1$ and $R_H \gg 1$ respectively. Buoyancy contours are shown in red at 1 m s^{-2} intervals from $b = 0.5$ m s^{-2}. The black line indicates the plume contour $\phi_p = 10^{-3}$.

4 | EXPLORING MODEL BEHAVIOUR

In this section we explore the behaviour of our minimal moisture model in two regimes, each with one of R_H or R_S varied, representing varying importance of the key microphysical processes. We vary the reference saturation concentration ϕ_0, yielding regimes with $R_H \gg 1, R_H \sim 1$ and $R_H \ll 1$, keeping all other parameters fixed (no sedimentation or shear). Separately, we vary the sedimentation velocity w_s, yielding regimes with $R_S \gg 1, R_S \sim 1$ and $R_S \ll 1$, keeping the plume forcing and ϕ_0 fixed and with no shear. All simulations are run to time $t_{\text{end}} = 15$ s (simulation value, corresponding to 10 minutes in the TTL) and plume forcing ends at time $t_{\text{lim}} = 10$ s (simulation value). Parameters for the simulations presented here are summarised in table 3. The focus here is solely on the behaviour of the model, how this depends on ϕ_0 and w_s, and the relation to the hydration mechanism in the TTL; a deeper discussion of the mechanisms and interactions in convective hydration of a stably stratified layer is given in Part II where we focus on the $R_H \gg 1$ regime.

4.1 | Flow evolution

Figure 3 shows snapshots of the simulations with varied reference saturation concentration ϕ_0 at $t = \frac{1}{3}\, t_{\text{end}}$ when the plume is rising towards its maximum penetration height, at $t = \frac{2}{3}\, t_{\text{end}}$ when the intrusion has begun to form and plume forcing ends, and at the simulation end time $t = t_{\text{end}}$. Each plot shows a cross-section through the plume centreline of the vapour concentration ϕ_v (left) and ice concentration ϕ_c (right) with buoyancy contours overlaid. Although plume forcing ends at time $t_{\text{lim}} = \frac{2}{3}\, t_{\text{end}}$, plume fluid continues to rise through the uniform layer up to the end of the simulation. Figure 3 illustrates how R_H relates to the partitioning of moisture into vapour and ice at penetration: when $R_H \ll 1$ there is very little ice in the plume throughout

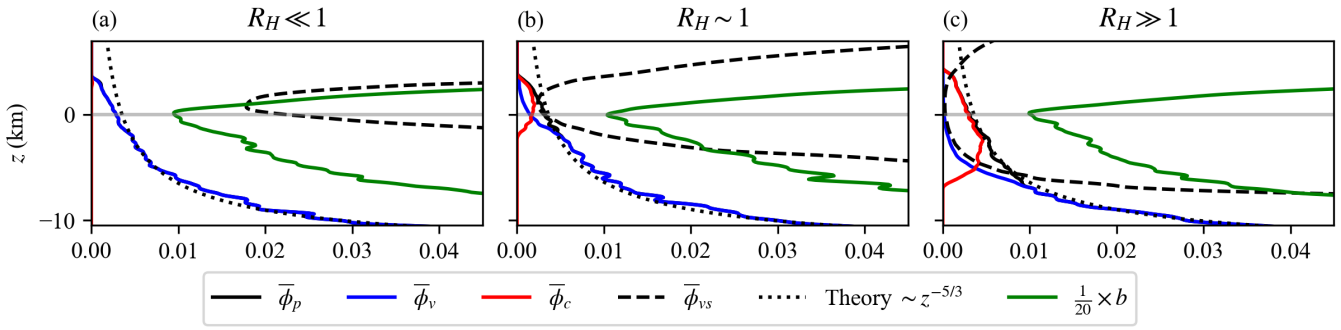

FIGURE 4 Vertical profiles of the time- and azimuthally-averaged tracer concentrations ϕ_p, ϕ_v, ϕ_c and saturation vapour concentration ϕ_{vs} on the plume centreline, averaged over $0 \leq t \leq t_{\text{lim}}$. Only the reference saturation concentration ϕ_0 is varied between simulations. The gray horizontal line indicates the 'cold point' $z = 0$ where the environmental temperature is minimised.

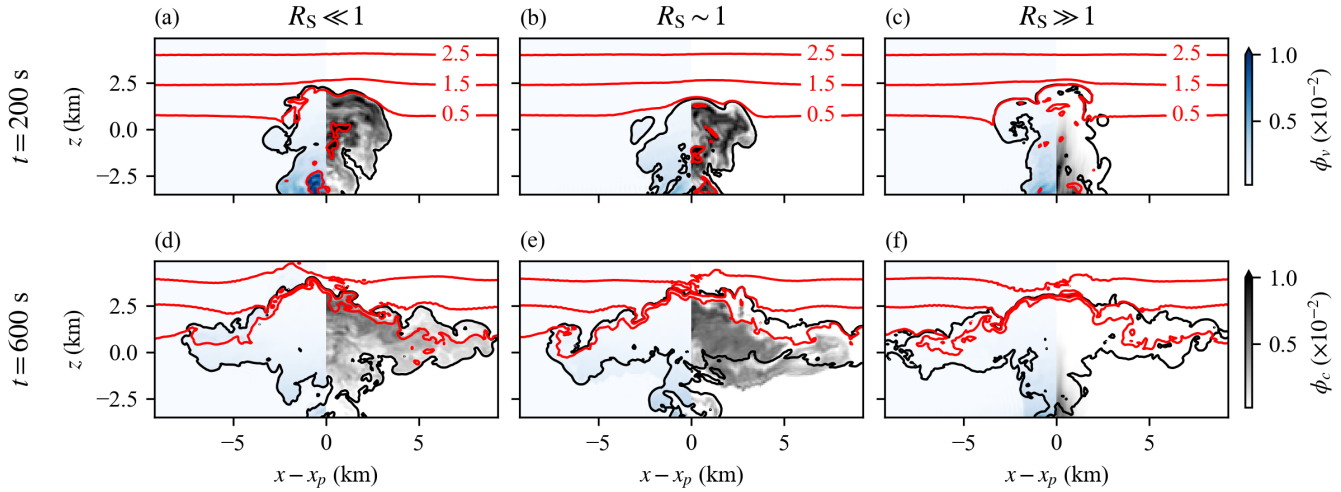

FIGURE 5 Snapshots of simulations with varied w_s at $t = \frac{1}{3} t_{\text{end}}$ and $t = t_{\text{end}}$ showing vapour ϕ_v and ice ϕ_c in each panel. These simulations are representative of regimes with $R_S \ll 1, R_S \sim 1$ and $R_S \gg 1$ respectively. Here, $R_H \approx 2$. Buoyancy contours are shown in red at 1 m s^{-2} intervals from $b = 0.5$ m s^{-2}. The black line indicates the plume contour $\phi_p = 10^{-3}$.

the stratified layer, other than a small amount that forms at the top of the plume due to adiabatic cooling as fluid rises to the maximum penetration height. Conversely, when $R_H \gg 1$, the plume penetrates into the stratified layer with most moisture in the form of ice. This effect is also seen using vertical profiles of the azimuthally averaged tracer concentrations $\overline{\phi}_p$, $\overline{\phi}_v$ and $\overline{\phi}_c$ on the plume centreline $r = 0$, as shown in figure 4. Fluid parcels rising through the plume on the centreline follow these profiles (on average), moving up the vertical axis as time increases. The averaged profiles shown in figure 4 do not fully reflect local changes in ϕ_{vs} from mixing between the plume and the significantly more buoyant surroundings, which could allow more substantial vapour concentrations to form. When the passive and vapour tracer concentration exceeds the saturation vapour concentration which decreases with height, ice is formed. As R_H increases from left to right in figure 4, we see that the height at which ice begins to form reduces and the ice concentration at penetration increases. Recall that without sedimentation, then $\phi_p = \phi_v + \phi_c$. A theoretical profile for the tracer concentration, based on the Morton et al. (1956) plume equations, is shown in the figure and corresponds well with the simulated profiles. The $R_H \gg 1$ simulation in figure 3(c), (f), (i) and figure 4(c) is representative of the TTL regime; plume fluid is 'freeze-dried' as it rises through the uniform layer, meaning that most vapour condenses to form ice. Thus the plume is loaded with ice at penetration. As buoyancy and temperature increases in the stratified layer, the saturation vapour concentration increases exponentially with height. Thus larger concentrations of vapour can exist at the top of the plume where plume and environmental fluid mix, so some of the ice carried by the plume sublimates to form vapour. In § 4.2 we use the volume distribution formalism introduced in § 3 to explore the 'hydration mechanism' in more detail.

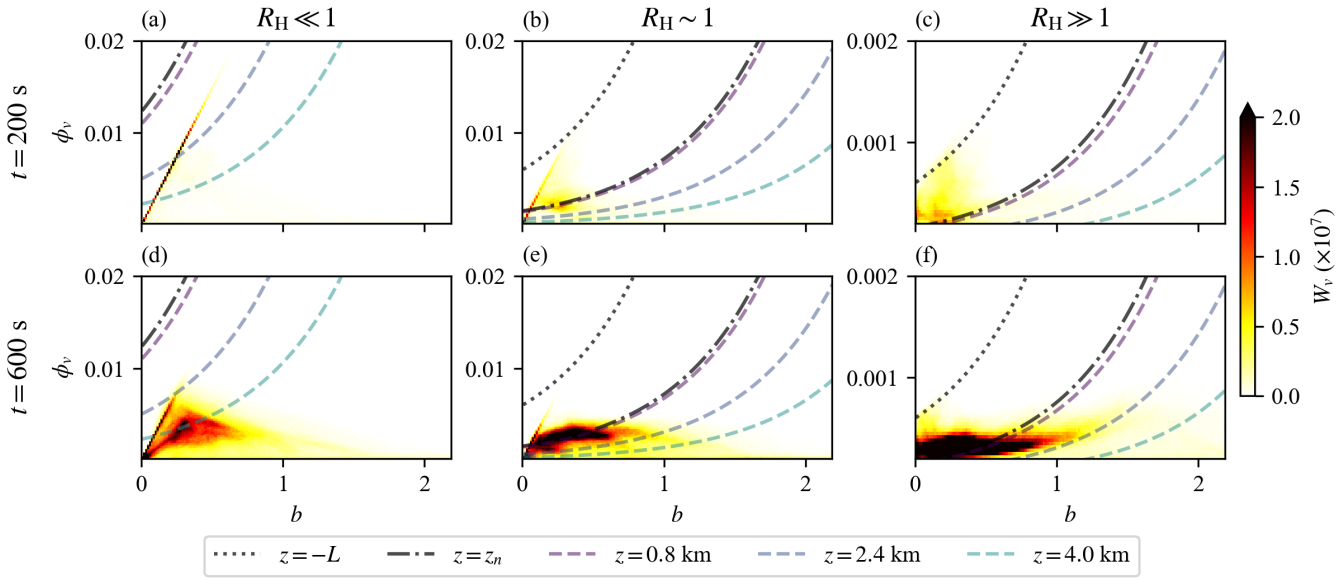

FIGURE 6 Buoyancy-vapour volume distribution W_v in simulations with $R_H \ll 1$, $R_H \sim 1$ and $R_H \gg 1$ at times $t = \frac{1}{3} t_{end}$ and $t = t_{end}$. Saturation curves $\phi_v = \phi_0 \exp(\alpha(\Theta b - \Gamma(z + H)))$ with $z = -L$ (black dotted), $z = z_n$ (black dot-dashed), and heights $z = 0.8, 2.4, 4.0$ km (dashed colour lines) corresponding to the $b = 0.5, 1.5, 2.5$ m s^{-2} contours in figure 3.

Figure 5 shows snapshots of the simulations with fixed reference saturation concentration $\phi_0 = 0.5$ and varied sedimentation velocity w_s. For these simulations, $R_H \approx 2$ so the $R_S \ll 1$ case (with very weak sedimentation) lies between the $R_H \sim 1$ and $R_H \gg 1$ regimes shown in figure 3, with both vapour and ice present in the plume at penetration, though the ice concentration is larger within the plume in the stratified layer because of adiabatic cooling during ascent to the maximum penetration height z_{max}. As the sedimentation velocity is weak in this case, there is little noticeable influence on the tracer concentrations in the plume. In the regime $R_S \gtrsim 1$, we have $w_s \gtrsim w_{eddy}$, so ice is 'decoupled' from the plume in the sense that we no longer have $\phi_p \approx \phi_v + \phi_c$ because ϕ_c does not precisely follow the flow. This can be seen at $t = t_{end}$ in the $R_S \sim 1$ and $R_S \gg 1$ cases, where ice has sedimented out of the plume into the subsaturated environment and sublimated to form vapour. Thus both vapour and ice are present outside of the $\phi_p = 10^{-3}$ contour that defines the plume. In these cases, we also see that little ice reaches the top surface of the plume cap (see figure 5(b) and (c)), where mixing between the plume and environment raises the temperature of fluid parcels. Thus the hydration mechanism detailed earlier is limited because only small amounts of ice are available to sublimate into vapour. Ice reaches the bottom of the stratified layer in both cases, even when the sedimentation velocity is much stronger than turbulent eddies as in the $R_S \gg 1$ case. This occurs because the vertical velocity on the plume centreline is significantly stronger than typical eddy velocities in the plume, so ice is still lifted into the stratified layer (unless w_s, hence R_S, is extremely large). However, once the updraft velocity weakens after penetration into the stratified layer, the mean flow is predominantly horizontal and the continued presence of ice in the plume is determined by R_S. In the $R_S \sim 1$ case, turbulent eddies keep most ice in suspension as the intrusion spreads radially, though some ice sediments out of the plume since w_{eddy} is only an average measure and some eddies are weaker than others. In the $R_S \gg 1$ case, turbulent eddies are – on average – too weak to keep ice in suspension, so almost all ice is lost immediately after penetration.

4.2 | Evolution of the moist distributions

We now use the volume distribution formalism introduced in § 3 to examine the effect of mixing on the vapour concentration in the regimes with varied R_H and R_S, demonstrating how the hydration mechanism operates when viewed in buoyancy-tracer space. In Part II we use this diagnostic approach to assess the influence of large-scale vertical shear on hydration via its influence on mixing. The crucial difference between the evolution of the buoyancy-vapour volume distribution W_v and the passive buoyancy-tracer volume distribution W_p is the influence of condensation which limits the vapour concentration to $\phi_v < \phi_{vs}$. In buoyancy-tracer space, this effect can be understood by considering the 'saturation curve' $\phi_{vs}(b; z) = \phi_0 \exp(\alpha(\Theta b - \Gamma(z + h)))$ as

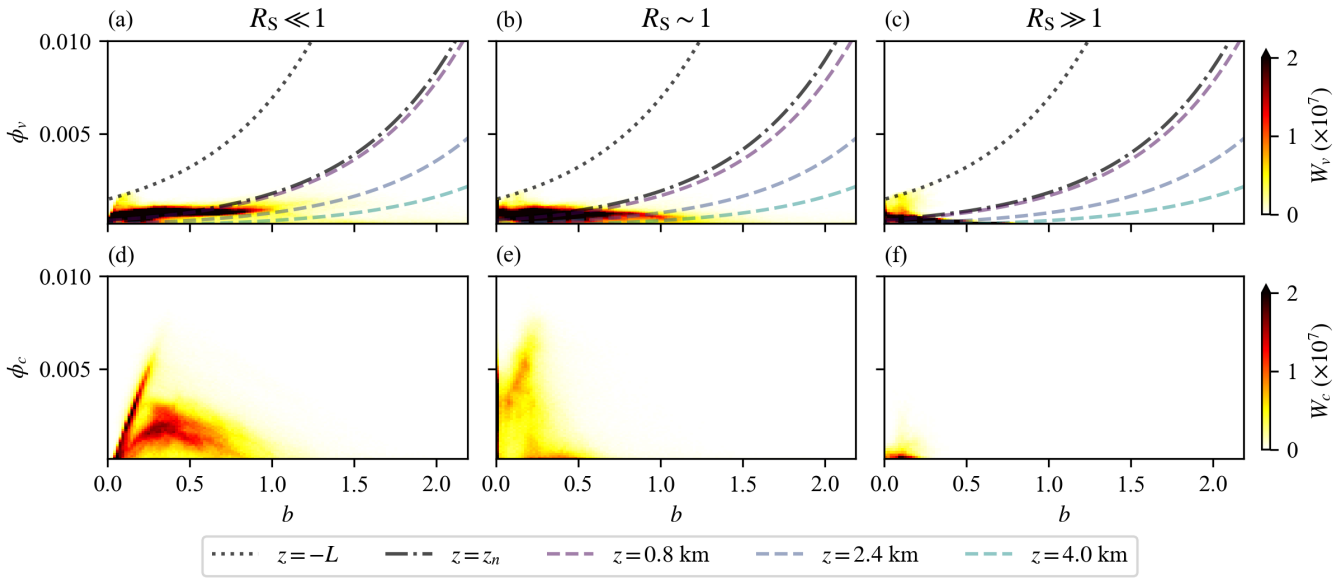

FIGURE 7 Buoyancy-vapour (top row) and buoyancy-ice (bottom row) volume distributions W_v and W_c in simulations with $R_S \ll 1, R_S \sim 1$ and $R_S \gg 1$ at time $t = t_{end}$. Saturation curves $\phi_v = \phi_0 \exp(\alpha(\Theta b - \Gamma(z + H)))$ with $z = -L$ (black dotted), $z = z_n$ (black dot-dashed), and heights $z = 0.8, 2.4, 4.0$ km (dashed colour lines) corresponding to the $b = 0.5, 1.5, 2.5$ m s^{-2} contours in figure 5.

a function of b at a given height z; fluid parcels at that height in physical space are restricted to lie below this curve in buoyancy-tracer space. Vapour that condenses forms ice which then sediments downwards. This reduces the ice concentration in a given fluid parcel and increases the parcel below it. Owing to the fact that fluid parcels associated with a region of buoyancy-tracer space are not necessarily co-located in physical space, it is difficult to interpret the sedimentation flux distribution K – we will revisit this point later. When sedimentation is weak so that ice remains in the stratified layer, the buoyancy-ice volume distribution W_c evolves in a qualitatively similar manner to the passive volume distribution W_p since there is no restriction on ice concentration. Some differences arise since the evolution indirectly depends on the buoyancy-vapour volume distribution, as ice is lost when the saturation vapour concentration increases (via mixing or changes in height). In terms of understanding vapour transport, it is therefore simplest to consider the buoyancy-vapour volume distribution W_v alone and to consider the effect of mixing on W_c (and other distributions) only where necessary.

Figure 6 shows W_v at $t = \frac{1}{3} t_{end}$ and $t = t_{end}$ in the simulations with $R_H \ll 1, R_H \sim 1$ and $R_H \gg 1$ and figure 7 shows W_v and W_c at $t = t_{end}$ in simulations with $R_S \ll 1, R_S \sim 1$ and $R_S \gg 1$. In each plot of W_v, we show the saturation curves $\phi_v = \phi_{vs}(b, z)$ for three illustrative values of z. Vapour concentrations exceeding the saturation curve at a given height will condense until ϕ_v reduces to the saturation value (with b unchanged). The black dotted line shows the saturation curve at $z = -L$ where the source distributions S_v and S_c are calculated and therefore acts as a limit on the maximum vapour concentrations at penetration. The black dash-dotted line shows the saturation curve at $z = z_n$ where the intrusion forms (i.e. the neutral buoyancy height); we expect vapour to accumulate near this curve at late times. The remaining coloured dashed lines show the saturation curve at heights that correspond with the buoyancy contours shown in the physical space cross-sections shown in figure 3 and figure 5.

Moist processes play essentially no role in the $R_H \ll 1$ simulation, so the vapour distribution W_v evolves in a qualitatively similar way to the passive distribution described in § 3.2. At all times, the vapour concentrations on the source line remain well below the saturation curves except for fluid with large b and ϕ_v at the end of the source line, which is shielded from the surroundings so vapour is condensed via adiabatic cooling during rise to z_{max}. In the $R_H \sim 1$ case most of the source line remains below the saturation curve at penetration, so condensation only occurs close to the plume centreline where vapour concentrations are large enough to exceed the saturation concentration. As fluid rises into the stratified layer, the saturation curve quickly limits vapour concentrations so most fluid parcels experience some condensation during rise towards z_{max}. As fluid parcels join the intrusion, they are limited by the saturation curves close to $z = z_n$ that limit the region of (b, ϕ_v) space where fluid can accumulate at late times.

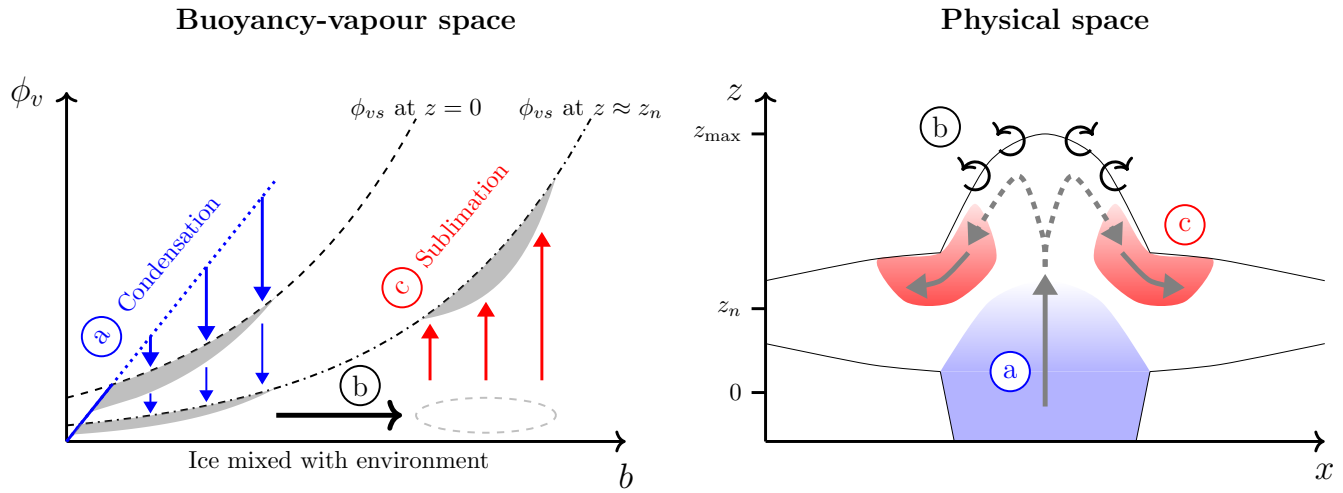

FIGURE 8 Schematic illustration of convective hydration of the stratified layer in the $R_H \gg 1$ regime where the plume is ice-loaded at penetration. Left panel shows processes in (b, ϕ_v)-space. Right panel shows corresponding effect in physical space with the flow indicated by solid gray arrows (when carrying vapour) and dashed gray arrows (without vapour). Coloured arrows in the left panel correspond with coloured regions in the right panel. (a) Plume fluid on the source line experiences condensation during rise through the uniform layer (blue arrows). At penetration, vapour concentrations (left, gray region at small b) are limited by the saturation curve with $z = 0$ (left, dashed black curve). (b) Ice carried by the plume is transported to larger buoyancies via mixing with more buoyant environmental fluid near $z_{\max}$ (left, gray dashed ellipse; right, circular arrows). Warmer mixed fluid permits larger vapour concentrations. (c) Sublimation of ice (red arrows) produces large vapour concentrations at large b (gray region at large b) which is aided by adiabatic warming as fluid descends and joins the intrusion. Fluid accumulates close to the saturation curve with $z = z_n$ (dot dashed black curve).

The evolution of W_v in the $R_H \gg 1$ is qualitatively different to the $R_H \ll 1$ and $R_H \sim 1$ cases: most fluid parcels undergo condensation during rise through the uniform layer so the evolution of W_v heavily depends on the evolution of W_c and subsequent conversion from ice back to vapour. The saturation curve at penetration significantly restricts vapour concentrations on the source line. Note the reduced scale for ϕ_v in panels (c) and (f) in figure 6 because there is very little direct transport of vapour into the stratified layer. As plume fluid mixes with the environment, ice and vapour is shifted towards larger b where the saturation concentration ϕ_{vs} is (exponentially) larger, allowing ice to sublimate. Thus W_v increases at large b via indirect transport through (b, ϕ_c)-space and without direct transport in (b, ϕ_v)-space. The abundance of ice in the $R_H \gg 1$ regime means that mixtures of plume and environmental fluid remain at saturation as ϕ_{vs} increases. Thus the volume distribution at $t = t_{\text{end}}$ accumulates near the saturation curve with $z = z_n$ at larger values of b than found in the $R_H \sim 1$ and $R_H \ll 1$ cases where the amount of ice is more limited. This process, which is representative of the TTL hydration mechanism (Powell et al., 2025), is illustrated schematically in figure 8.

In the simulation with $R_S \ll 1$ we see similar behaviour to the $R_H \gg 1$ simulation but when R_S increases the region of (b, ϕ_v) space where fluid accumulates is gradually restricted to smaller values of b and ϕ_v. Ice settles out of the plume before it can be mixed to larger b (see W_c in panel (e) and (f) of figure 7), thus limiting the effectiveness of mixing with the environment in producing vapour via sublimation. Instead, vapour concentrations are reduced because of dilution with dry environmental fluid.

For completeness, figure 9 shows the remaining distributions J_c, J_v, K as well as the cumulative source distributions for vapour $\int S_v \, dt$ and ice $\int S_c \, dt$ at a single time $t = \frac{2}{3} t_{\text{end}}$ in the $R_S \sim 1$ regime. The cumulative source distributions are time-integrated forms of the source distributions, which empirically illustrate the 'source line' discussed in § 3 that represents the characteristics of plume fluid at penetration. The source line is relatively diffuse for the ice tracer in figure 9(b) since it is not forced in the plume, so ice only forms when vapour condenses, and the amount of ice formed varies depending on the extent to which ϕ_v exceeds ϕ_{vs}. The source line for the vapour tracer in figure 9(c) is well defined, as with the passive tracer, but the extreme end where b and ϕ_v are largest is limited by the saturation curve at penetration.

As stated earlier, the sedimentation, sublimation and condensation fluxes are difficult to interpret since they represent a conversion between two different phase spaces. Regions where the condensation flux J_v is positive in (b, ϕ_v) space shows where vapour is being converted to ice (blue), which appears in (b, ϕ_c) space where J_c is positive (red). Similarly, J_v is positive

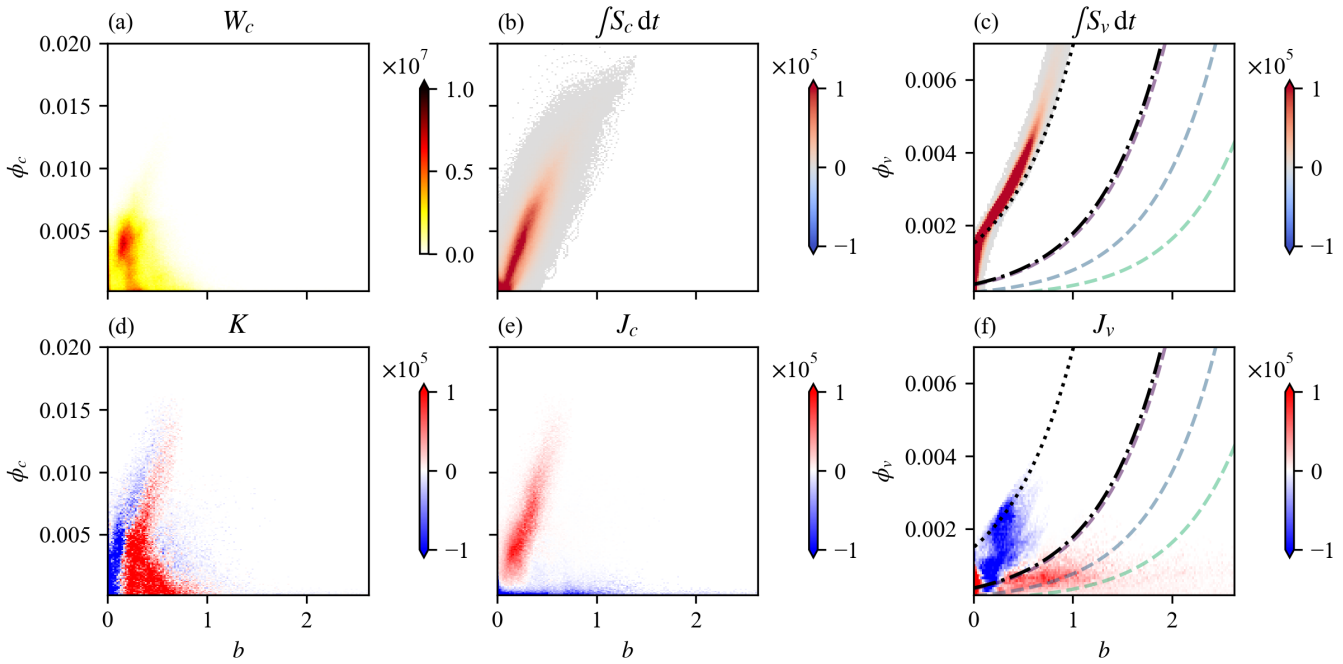

FIGURE 9 Ice tracer volume distribution W_c, cumulative source ice and vapour distributions $\int S_c\,\mathrm{d}t$ and $\int S_v\,\mathrm{d}t$, sedimentation flux K, sublimation flux J_c, and condensation flux J_v at $t = \frac{2}{3}\,t_{\mathrm{end}}$ in the simulation with $R_S \sim 1$. In the two rightmost panels showing (b, ϕ_v) space, saturation curves are shown as in figure 6 and 7.

(red) where ice is being sublimated and corresponds with regions where J_c is negative (blue). This is consistent with the schematic illustration of the hydration process in figure 8 – ice is formed on the source line as the saturation curve limits vapour concentrations during ascent, which is then mixed towards large buoyancy via mixing with the more buoyant environment, and then sublimated to reach saturation at larger b where larger vapour concentrations are permitted. Alongside the moist conversion processes, sedimentation moves ice downwards. Figure 9(d) shows the sedimentation flux distribution K with the buoyancy-ice volume distribution W_c shown in figure 9(a) for reference. We see that K is negative at the extreme end of the source line where b and ϕ_c are larger, since the volume of fluid with these larger concentrations is reduced as ice sediments out of the plume. Correspondingly, the volume of fluid with smaller concentrations of ice increases so K is positive where ϕ_c is smaller.

5 | CONCLUSION

In this paper we have formulated an idealised model for hydration of the TTL by overshooting convection. Overshooting tops are modelled as a buoyant plume penetrating from a uniform layer into a linearly stably stratified layer. We model moisture transport using a passive tracer carried by the flow together with two temperature-dependent tracers representing vapour and ice. The vapour concentration is limited by the saturation vapour concentration; excess vapour condenses to form ice that sediments at a fixed velocity. The model uses the fast condensation limit in which moist processes are fast compared to the dynamics. Consistent with the Boussinesq numerical scheme (valid given the shallow region of interest), we adopt a Boussinesq representation of temperature to formulate the saturation vapour concentration, following Vallis et al. (2019). In this paper we have formulated the numerical model and validated its behaviour whilst introducing diagnostic approaches to understand the flow.

To understand the influence of mixing on vapour transport we extended the buoyancy-vapour volume distribution formalism introduced in Powell et al. (2024), which maps the flow from physical space to a phase space which represents the volume of fluid with given values of buoyancy and tracer concentration. This ‘volume distribution’ is invariant under advection and modified only by mixing, sedimentation, and exchange between the two moist tracers. The approach is valuable given the importance of simultaneous changes in buoyancy and tracer concentration as a result of turbulent mixing in a stratified flow. Our diagnostic approach also provides a straightforward framework for understanding the mechanism for convective hydration of a stratified layer using a geometric argument which limits the evolution of the buoyancy-vapour volume distribution with ‘saturation curves’.

This characterises the indirect vapour transport whereby vapour condenses to form ice that is then mixed with environmental fluid to become more buoyant (and warmer), raising the saturation concentration and allowing ice to sublimate to form vapour. Thus vapour is formed in the stratified layer indirectly by transporting ice in the plume, even without direct transport of vapour.

The behaviour of our idealised model was explored using experiments in which the sedimentation velocity and saturation vapour concentration were independently varied to control the influence of ice sedimentation and the extent to which condensation occurs as the plume rises through the uniform layer. These experiments showed that sedimentation influences vapour transport by determining whether ice is kept in suspension once fluid reaches the plume cap. The large vertical velocity in the rising plume is sufficient to lift ice into the stratified layer, but the typical turbulent eddy velocity determines whether ice remains in suspension as fluid rises into the plume cap and overturns. The most effective mixing between the plume and environment occurs during overturning since this is where plume fluid is exposed to the most buoyant (i.e. warmest) environmental fluid.

In Part II, we restrict attention to the $R_H \gg 1$ regime representative of the TTL, in which the plume penetrates the stratified layer carrying large amounts of ice and relatively little vapour. Further experiments are performed to explore the influence of mixing, sedimentation, convective intensity and large-scale vertical shear on convective hydration of a stratified layer. Using a model which retains only the essential physical mechanisms allows more straightforward interpretation of the interaction between different processes. The use of large-eddy simulations of a scaled-down flow permits exploration of a wider range of regimes at a practical computation cost compared with comprehensive meteorological models that retain more realistic representations of physical processes and complex environmental setups. Our study also features a more realistic representation of turbulence owing to increased resolution of the turbulent spectrum and an improved sub-grid-scale scheme, compared to previous cloud-resolving studies that parameterised most of the turbulent spectrum.

ACKNOWLEDGMENTS

CWP acknowledges funding from EPSRC grant EP/T517846/1.

CONFLICT OF INTEREST

The authors declare no potential conflict of interests.

DATA AVAILABILITY STATEMENT

Simulation data and scripts used to generate figures are available upon request.

References

Abkar, M., Bae, H.J. & Moin, P. (2016) Minimum-dissipation scalar transport model for large-eddy simulation of turbulent flows. *Phys. Rev. Fluids*, 1(4), 041701. doi:10.1103/PhysRevFluids.1.041701.

Dauhut, T., Chaboureau, J.P., Escobar, J. & Mascart, P. (2015) Large-eddy simulations of Hector the convector making the stratosphere wetter. *Atmospheric Science Letters*, 16(2), 135–140. doi:10.1002/asl2.534.

Dauhut, T., Chaboureau, J.P., Haynes, P. & Lane, T. (2018) The Mechanisms Leading to a Stratospheric Hydration by Overshooting Convection. *J. Atmospheric Sci.*, 75. doi:10.1175/JAS-D-18-0176.1.

Dauhut, T. & Hohenegger, C. (2022) The Contribution of Convection to the Stratospheric Water Vapor: The First Budget Using a Global Storm-Resolving Model. *JGR Atmospheres*, 127(5), e2021JD036295. doi:10.1029/2021JD036295.

DeBonis, J.R. (2019) *WRLES: Wave Resolving Large-Eddy Simulation Code, Theory and Usage*. Glenn Research Center, Cleveland, Ohio. 2019-220192.

Devenish, B.J., Rooney, G.G. & Thomson, D.J. (2010) Large-eddy simulation of a buoyant plume in uniform and stably stratified environments. *J. Fluid Mech.*, 652, 75–103. doi:10.1017/S0022112010000017.

Feist, M.M., Westbrook, C.D., Clark, P.A., Stein, T.H., Lean, H.W. & Stirling, A.J. (2019) Statistics of convective cloud turbulence from a comprehensive turbulence retrieval method for radar observations. *Quart J Royal Meteoro Soc*, 145(719), 727–744. doi:10.1002/qj.3462.

Frisch, U. (1995) *Turbulence: The Legacy of A.N. Kolmogorov*, 1st Edition. : Cambridge University Press.

Gelb, A. & Gottlieb, S. (2007) The Resolution of the Gibbs Phenomenon for Fourier Spectral Methods. *Adv. Gibbs Phenom. Sampl. Publ. Potsdam N. Y.*,.

Grabowski, W.W. (1998) Toward Cloud Resolving Modeling of Large-Scale Tropical Circulations: A Simple Cloud Microphysics Parameterization. *J. Atmos. Sci.*, 55(21), 3283–3298. doi:10.1175/1520-0469(1998)055<3283:TCRMOL>2.0.CO;2.

Hassim, M.E.E. & Lane, T.P. (2010) A model study on the influence of overshooting convection on TTL water vapour. *Atmos. Chem. Phys.*, 10(20), 9833–9849. doi:10.5194/acp-10-9833-2010.

Hernandez-Duenas, G., Majda, A.J., Smith, L.M. & Stechmann, S.N. (2013) Minimal models for precipitating turbulent convection. *J. Fluid Mech.*, 717, 576–611. doi:10.1017/jfm.2012.597.

Jensen, E.J., Ackerman, A.S. & Smith, J.A. (2007) Can overshooting convection dehydrate the tropical tropopause layer? *J. Geophys. Res.*, 112(D11), 2006JD007943. doi:10.1029/2006JD007943.

Jensen, E.J., Pan, L.L., Honomichl, S., Diskin, G.S., Krämer, M., Spelten, N. et al. (2020) Assessment of Observational Evidence for Direct Convective Hydration of the Lower Stratosphere. *JGR Atmospheres*, 125(15), e2020JD032793. doi:10.1029/2020JD032793.

Khain, A.P., Beheng, K.D., Heymsfield, A., Korolev, A., Krichak, S.O., Levin, Z. et al. (2015) Representation of microphysical processes in cloud-resolving models: Spectral (bin) microphysics versus bulk parameterization. *Reviews of Geophysics*, 53(2), 247–322. doi:10.1002/2014RG000468.

Khaykin, S., Lukyanov, A. & Williams, E. (2009) Hydration of the lower stratosphere by ice crystal geysers over land convective systems. *Atmos. Chem. Phys.*,.

Khaykin, S.M., Moyer, E., Krämer, M., Clouser, B., Bucci, S., Legras, B. et al. (2022) Persistence of moist plumes from overshooting convection in the Asian monsoon anticyclone. *Atmos. Chem. Phys.*, 22(5), 3169–3189. doi:10.5194/acp-22-3169-2022.

Morton, B.R., Taylor, G.I. & Turner, J.S. (1956) Turbulent gravitational convection from maintained and instantaneous sources. *Proc. R. Soc. Lond. A*, 234(1196), 1–23. doi:10.1098/rspa.1956.0011.

Nugent, J.M. & Bretherton, C.S. (2023) Tropical Convection Overshoots the Cold Point Tropopause Nearly as Often Over Warm Oceans as Over Land. *Geophysical Research Letters*, 50(21), e2023GL105083. doi:10.1029/2023GL105083.

Pan, L.L., Honomichl, S.B., Thornberry, T., Rollins, A., Bui, T.P., Pfister, L. et al. (2019) Observational Evidence of Horizontal Transport-Driven Dehydration in the TTL. *Geophysical Research Letters*, 46(13), 7848–7856. doi:10.1029/2019GL083647.

Penney, J., Morel, Y., Haynes, P., Auclair, F. & Nguyen, C. (2020) Diapycnal mixing of passive tracers by Kelvin–Helmholtz instabilities. *J. Fluid Mech.*, 900, A26. doi:10.1017/jfm.2020.483.

Powell, C.W., Haynes, P.H., Ming, A.D. & Taylor, J.R. (2025) Moisture transport by convective overshoots in the tropical tropopause layer. *Weather*, 80, wea.7689. doi:10.1002/wea.7689.

Powell, C.W., Haynes, P.H. & Taylor, J.R. (2024) Diagnosing tracer transport in convective penetration of a stably stratified layer. *J. Fluid Mech.*, 997, A48. doi:10.1017/jfm.2024.662.

Randel, W. & Park, M. (2019) Diagnosing Observed Stratospheric Water Vapor Relationships to the Cold Point Tropical Tropopause. *JGR Atmospheres*, 124(13), 7018–7033. doi:10.1029/2019JD030648.

Randel, W.J. & Jensen, E.J. (2013) Physical processes in the tropical tropopause layer and their roles in a changing climate. *Nat. Geosci.*, 6(3), 169–176. doi:10.1038/ngeo1733.

Randel, W.J., Wu, F., Oltmans, S.J., Rosenlof, K. & Nedoluha, G.E. (2004) Interannual Changes of Stratospheric Water Vapor and Correlations with Tropical Tropopause Temperatures. *J. Atmos. Sci.*, 61(17), 2133–2148. doi:10.1175/1520-0469(2004)061<2133:ICOSWV>2.0.CO;2.

Rogers, R.R. & Yau, M.K. (1989) *A Short Course in Cloud Physics*. : Butterworth-Heinemann.

Rossow, W.B. & Pearl, C. (2007) 22-Year survey of tropical convection penetrating into the lower stratosphere. *Geophysical Research Letters*, 34(4), 2006GL028635. doi:10.1029/2006GL028635.

Sang, W., Huang, Q., Tian, W., Wright, J.S., Zhang, J., Tian, H. et al. (2018) A Large Eddy Model Study on the Effect of Overshooting Convection on Lower Stratospheric Water Vapor. *JGR Atmospheres*, 123(18). doi:10.1029/2017JD028069.

Schoeberl, M.R., Dessler, A.E., Wang, T., Avery, M.A. & Jensen, E.J. (2014) Cloud formation, convection, and stratospheric dehydration. *Earth and Space Science*, 1(1), 1–17. doi:10.1002/2014EA000014.

Taylor, J. (2008) Numerical Simulations of the Stratified Oceanic Bottom Boundary Layer. Ph.D. thesis, University of California, San Diego.

Ueyama, R., Jensen, E.J. & Pfister, L. (2018) Convective Influence on the Humidity and Clouds in the Tropical Tropopause Layer During Boreal Summer. *JGR Atmospheres*, 123(14), 7576–7593. doi:10.1029/2018JD028674.

Ueyama, R., Jensen, E.J., Pfister, L. & Kim, J.E. (2015) Dynamical, convective, and microphysical control on wintertime distributions of water vapor and clouds in the tropical tropopause layer. *J. Geophys. Res.*, 120(19), 10483–10500. doi:10.1002/2015JD023318.

Vallis, G.K., Parker, D.J. & Tobias, S.M. (2019) A simple system for moist convection: The Rainy–Bénard model. *J. Fluid Mech.*, 862, 162–199. doi:10.1017/jfm.2018.954.

Vreugdenhil, C.A. & Taylor, J.R. (2018) Large-eddy simulations of stratified plane Couette flow using the anisotropic minimum-dissipation model. *Physics of Fluids*, 30(8), 085104. doi:10.1063/1.5037039.

Wright, J.S., Fu, R., Fueglistaler, S., Liu, Y.S. & Zhang, Y. (2011) The influence of summertime convection over Southeast Asia on water vapor in the tropical stratosphere. *J. Geophys. Res.*, 116(D12), D12302. doi:10.1029/2010JD015416.